Germanium-on-silicon Vernier-effect photonic microcavities for the mid-infrared

Original Citation:
Germanium-on-silicon Vernier-effect photonic microcavities for the mid-infrared / Troia, Benedetto; Nedeljkovic, M.; Khokhar, A.; Soler Penades, J.; Alonso Ramos, C.; Passaro, Vittorio; Mashanovich, G. Z.. - In: OPTICS LETTERS. - ISSN 0146-9592. - ELETTRONICO. - 41:3(2016), pp. 610-613. [10.1364/OL.41.000610]

Availability:
This version is available at http://hdl.handle.net/11589/88198 since: 2022-06-23

Published version
DOI:10.1364/OL.41.000610

Germanium-on-silicon Vernier-effect photonic microcavities for the mid-infrared

BENEDETTO TROIA,[1] JORDI SOLER PENADES,[2] ALI Z. KHOKHAR,[2]
MILOS NEDELJKOVIC,[2] CARLOS ALONSO-RAMOS,[3] VITTORIO M. N. PASSARO,[1,*]
AND GORAN Z. MASHANOVICH[2]

[1]Department of Electrical and Information Engineering, Politecnico di Bari, Via E. Orabona 4, 70125 Bari, Italy
[2]Optoelectronics Research Centre, University of Southampton, Southampton SO17 1BJ, UK
[3]Institut d'Electronique Fondamentale, Université Paris-Sud CNRS UMR 8622, Université Paris-Saclay F-91405 Orsay, France
*Corresponding author: vittorio.passaro@poliba.it

Received XX Month XXXX; revised XX Month, XXXX; accepted XX Month XXXX; posted XX Month XXXX (Doc. ID XXXXX); published XX Month XXXX

We present Vernier-effect photonic microcavities based on germanium-on-silicon technology platform, operating around the mid-infrared wavelength of 3.8 μm. Cascaded racetrack resonators have been designed to operate in the second regime of the Vernier effect and typical Vernier comb-like spectra have been successfully demonstrated with insertion losses of ~5 dB, maximum extinction ratios of ~23 dB and loaded quality factors higher than 5,000. Furthermore, an add-drop racetrack resonator designed for a Vernier device has been characterized, exhibiting average insertion losses of 1 dB, extinction ratios of up to 18 dB and a quality factor of ~1,700. © 2015 Optical Society of America

OCIS codes: *(130.3120) Integrated optics devices; (130.3060) infrared; (230.4555) coupled resonators; (230.5750) resonators.*

http://dx.doi.org/10.1364/OL.99.099999

Germanium (Ge) is currently seen as one of the most promising group IV materials for extending the operation of photonic circuits from the near- to the mid-infrared (NIR and MIR, respectively). Ge offers a number of inherent advantages such as a broad transmission in the wavelength range of 2-14 μm, where fingerprints of a large number of chemical and biochemical species can be identified via vibrational spectroscopy. Ge also exhibits a higher nonlinear coefficient and a larger carrier mobility than silicon (Si), while still offering compatibility with standard photolithography and etching methods. So far, low-loss monocrystalline waveguides on germanium-on-silicon (Ge-on-Si) technology platform have been demonstrated at MIR wavelengths up to 5.8 μm with propagation losses of 3.6 ± 0.8 dB/cm and bending loss of 0.12 dB/90° with a radius of 115 μm [1], while record low propagation loss of 0.6 dB/cm has been demonstrated at 3.8 μm [2]. Moreover, a Ge-on-Si DEMUX based on planar concave gratings [3] and a MUX based on arrayed waveguide gratings [4] have been demonstrated at the wavelength range of 5.0-5.4 μm. Very recently, Ge-on-Si and Ge-on-silicon-on-insulator (Ge-on-SOI) thermo-optic phase shifters have been fabricated and characterized at 5 μm [5], while all-optical modulation [6] and two-photon absorption measurements [7] have also been reported. Finally, theoretical results on free carrier modulation in Ge [8], as well as on Ge-based Raman lasers and supercontinuum generation in Ge-on-Si waveguides at wavelengths in the range of 3-5 μm [9,10] have been recently reported.

Serially coupled multiple ring resonator filters (SMRRs) are useful to broaden the free spectral range (FSR) to the least common multiple of the FSR of individual ring resonators (RRs). This can be achieved by choosing different radii of the individual resonators in the SMRR, that is called the Vernier operation [11]. Actually, Vernier devices operating in the second regime of the Vernier effect have been widely used for refractive index (RI) sensing in the NIR. In particular, ultra-high sensing performance, such as wavelength sensitivities up to 460 μm/RIU (refractive index unit) and limits of detection (LOD) of the order of 10^{-6} RIU have been achieved by means of Vernier configurations constituted by cascade-coupled RRs, Mach-Zehnder interferometers and combinations of both, as reported in Table 1 of Ref. [12]. In this context, by extending the operation of Vernier devices into the MIR, sensing functionalities can be dramatically improved by employing both RI and optical absorption sensing principles simultaneously. Furthermore, typical comb-like Vernier spectra can be engineered as a function of the specific analyte to be sensed and Vernier devices can be efficiently employed for MIR real-time spectroscopy.

We have previously demonstrated Vernier spectra in the MIR, around 3.8 μm, in cascade-coupled RRs based on SOI rib [13] and fully-etched waveguides [14]. So far, optical absorption based sensing functionalities have been demonstrated for cocaine detection in a Ge-on-Si sensor characterized by a straight strip waveguide operating at 5.8 μm, where cocaine exhibits a strong absorption peak [15]. However, the smallest detected concentration of cocaine was 100 μg ml^{-1}, whereas state-of-the-art LODs reported in the NIR can be as low as ng ml^{-1}. Consequently, a library of high-performance Ge-based sensing devices operating in the MIR is strongly required in order to achieve performance competitive with NIR counterpart devices, and to even go beyond it towards innovative MIR lab-on-a-chip applications.

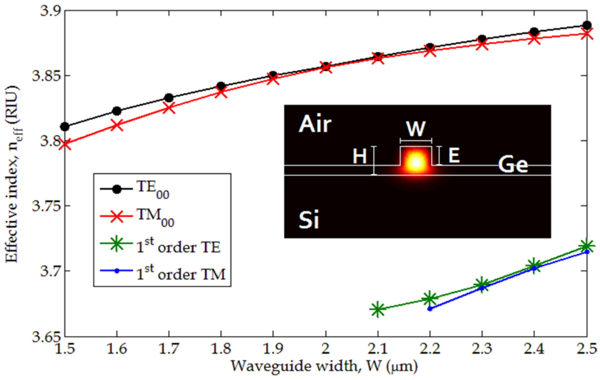

Fig. 1. Mode analysis of Ge-on-Si rib waveguide with fixed dimensions H = 2 μm, E = 1.35 μm, at λ = 3.8 μm. The simulated optical spatial distribution of the E_x component of the fundamental TE-polarized mode with W = 2.2 μm is plotted in the inset.

In this Letter, we report the experimental demonstration of Vernier effect in RRs based on Ge-on-Si rib waveguides and operating around 3.8 μm. Sophisticated algorithmic procedures based on custom-made codes and the finite element method (FEM) that we have developed for the design and fabrication of SOI Vernier architectures [16] and guided-wave optical directional couplers [17], already tested efficiently in the MIR [13,14] and NIR [12], have also been used here and adapted to the Ge-on-Si technology platform.

The devices are based on Ge-on-Si rib waveguides with height H = 2 μm, width W = 2.2 μm, and etch depth E = 1.35 μm. The waveguide mode analysis is plotted in Fig. 1 and simulation results evidence that high-order modes i.e., the 1st order TE (transverse electric) and the 1st order TM (transverse magnetic), start propagating at widths of 2.1 μm and 2.2 μm, respectively. However, they do not interfere with the propagation of the fundamental modes in the designed waveguides as they are too lossy at W = 2.2 μm. It is worth specifying that, although the difference between the effective indices of the fundamental modes (i.e., $\Delta n_{eff} = n_{eff,TE_{00}} - n_{eff,TM_{00}}$) is as low as 2×10^{-3} RIU at W = 2.2 μm, the use of a polarization controller and grating couplers designed for TE coupling ensured that only the TE_{00} mode was propagating. Fabrication tolerances for the width W and the etch depth E of ± 20 nm have been taken into account in the design procedure, resulting in maximum group index variations of $n_g \approx 4.2 \pm 1\times10^{-3}$. Moreover, chromatic dispersion in the 3.7-3.9 μm range has been included in the simulations by means of Ge and Si Sellemeier equations [18].

A set of RR lengths varied in the range of 400-1300 μm with a step of 0.05 μm was processed, resulting in 74 different Vernier configurations [12,16]. The lower and upper limit lengths were chosen in order to achieve low bending loss with the shortest radius and a minimum FSR properly measurable by our setup, with the longest roundtrip length, respectively. Then, we have selected the devices #A and #B in order to investigate the influence of considerably different RR radii and lengths on Vernier operation. Actually, each device is characterized by the RR pair [RR #A1, RR #A2] in Vernier #A and [RR #B1, RR #B2] in Vernier #B and their geometrical dimensions, i.e., RR lengths, L, and radii, R, as well as the lengths of the straight waveguide sections of the directional couplers, L_i, and the directional coupler gaps, g_0, are listed in Table 1. In particular, the four directional couplers of each Vernier device have been designed in order to exhibit power coupling coefficients, κ_c^2, less than 0.1 and as equal to each other as possible in order to achieve high extinction ratios in Vernier spectra. Then, each add-drop RR has been designed with symmetric directional couplers, i.e., identical L_i and g_0.

Table 1. Geometrical parameters of Vernier #A and Vernier #B architectures.

Parameters	Vernier #A		Vernier #B	
	RR #A1	RR #A2	RR #B1	RR #B2
L (μm)	439.60	449.60	1039.30	1079.10
R (μm)	59	59	142	149
L_i (μm)	34.44	39.44	73.54	71.45
g_0 (nm)	450	450	650	650

Cascade-coupled RR lengths, which are crucial design and fabrication parameters, have been calculated in order to satisfy the condition for operating in the second Vernier regime [16]:

$$\Delta FSR = |FSR_{RR\,\#1} - FSR_{RR\,\#2}| < \Delta\lambda_{FWHM(RR\,\#1,RR\,\#2)}. \qquad \textbf{(1)}$$

In Eq. (1), $FSR_{RR\,\#i}$ (i = 1,2) and $\Delta\lambda_{FWHM(RR\,\#1,RR\,\#2)}$ are the FSRs of the cascade-coupled add-drop RRs and the smallest full-width at half maximum (FWHM) of resonant peaks of individual RRs of the Vernier architecture, respectively.

As can be predicted by Eq. (1), the operation of Vernier architectures in the second regime is not significantly influenced by propagation losses because the higher the loss, the wider $\Delta\lambda_{FWHM}$, thus Eq. (1) is always satisfied. However, they can affect insertion losses and extinction ratios in Vernier and single RR spectra. It is therefore worth specifying that a bending loss of 0.046 dB/90° has been estimated by using a film mode matching (FMM) solver, in the case of R = 59 μm, i.e., the shortest radius among Vernier #A and Vernier #B RRs, while negligible losses (10^{-7} dB/90°) resulted for bends with radii of 142 μm and 149 μm. Also, bend losses of 1.3 dB/90° and 0.435 dB/90° have been calculated in the case of R = 30 μm and R = 40 μm, respectively. By considering bending losses that we measured in SOI rib waveguides (H = 0.4 μm, E = 0.22 μm, W = 1.35 μm) at 3.75 μm [13], i.e., 0.073 (R = 20 μm), 0.06 (R = 30 μm) and 0.033 (R = 40 μm) dB/90°, simulation results suggest that the influence of bends in Ge-on-Si RRs can be much stronger due to the larger Ge-on-Si waveguide dimensions that result from the smaller RI contrast between Si and Ge (i.e., ~ 0.6) compared to that of Si and the oxide (i.e., ~ 2). Finally, the shallower the etch depth in the Ge-on-Si rib waveguide (Fig. 1), the higher the bending losses. For example, 0.633 and 5×10^{-4} dB/90° have resulted, assuming E = 1.25 μm and E = 1.45 μm, respectively, with the radius R = 59 μm.

The devices were fabricated on a 2 μm Ge-on-Si sample spin coated

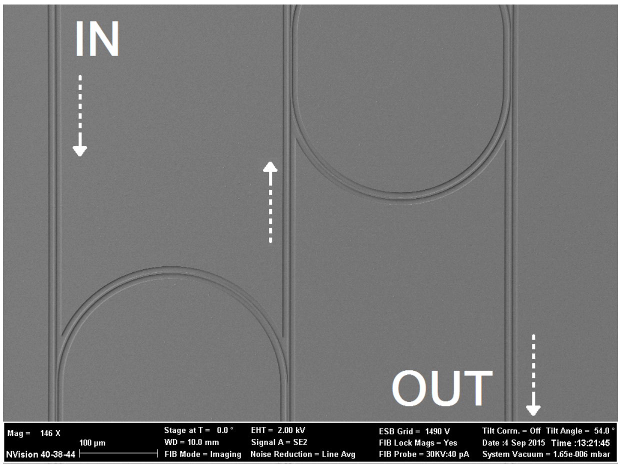

Fig. 2. Top view SEM image of a representative Ge-on-Si Vernier device consisting of two cascade-coupled add-drop racetrack resonators. Input and output ports are labeled, while the direction of light propagation is indicated by dotted arrows.

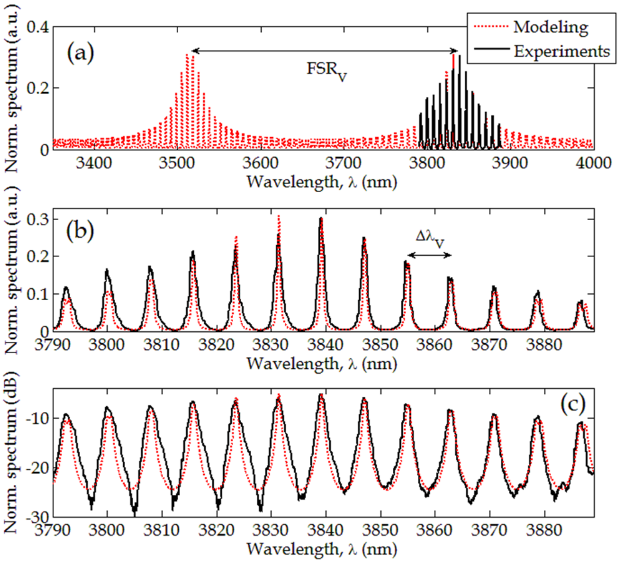

Fig. 3. (a) Theoretical and experimental spectra of Vernier #A device in a broad spectral range. Vernier #A spectra plotted in a narrow spectral range in (b) a.u. and (c) dB scale.

with ZEP-520A positive resist and patterned by a JEOL JBX 9300FS e-beam lithography tool. The chip was later dry etched in an Oxford Instruments ICP 380 plasma system using SF$_6$ and C$_4$F$_8$ gases [2].

Figure 2 shows the scanning electron microscope (SEM) top view image of a representative Vernier device with input/output ports and light propagation direction labeled in. The input, middle, and output bus waveguides were terminated by grating couplers that were designed specifically for TE-polarized light, and which were used to characterize the device.

The experimental setup described in [19] was used to characterize Vernier architectures and single add-drop RRs. A tunable quantum cascade laser (QCL) emitting at wavelengths in the range of 3.7-3.9 µm was used with a spectral sampling step of 0.02 nm for experimental data acquisition.

A typical comb-like Vernier spectrum in the second operating regime is the result of the product of the cascade-coupled add-drop RR transmittances. A number of adjacent resonances separated by a spectral distance $\Delta\lambda_V$ constitute the overall Vernier peaks, which are separated by the Vernier FSR, FSR_V. $\Delta\lambda_V$ is equal to the shortest FSR of the cascaded RRs, while FSR_V can be calculated as $(FSR_{RR\,\#1} \cdot FSR_{RR\,\#2})/\Delta FSR$. Another important figure of merit of Vernier devices designed for sensing applications is the Vernier gain, G_V, defined as the ratio $FSR_{RR\,\#1}/\Delta FSR$. When a Vernier device is designed to operate as a sensor, it must be covered by an insulating layer and a sensitive window must be opened above only one of the two RRs so that it can be exposed to the analyte to be sensed [16]. Under this hypothesis, $FSR_{RR\,\#1}$ mentioned in the definition of G_V is the FSR of the isolated RR. Although at this stage we did not consider any insulating layer on top of the Vernier devices as we are aiming first to develop a mature technology platform, the formula of G_V is still valid.

Table 2. Optical parameters and performance of Vernier #A and Vernier #B architectures.

Parameters	Vernier #A		Vernier #B	
	RR #A1	RR #A2	RR #B1	RR #B2
FSR (nm)	7.82	7.64	3.31	3.18
κ_c^2	0.042	0.051	0.068	0.066
IL_V (dB)	5.17		5.42	
ER_V (dB)	20.45		15.00	
Q_V	3,147		5,361	
$\Delta\lambda_V$ (nm)	~ 7.50		~ 3.10	
ΔFSR (nm)	0.18		0.13	
FSR_V (nm)	331.91		80.96	
G_V	43.44		25.46	

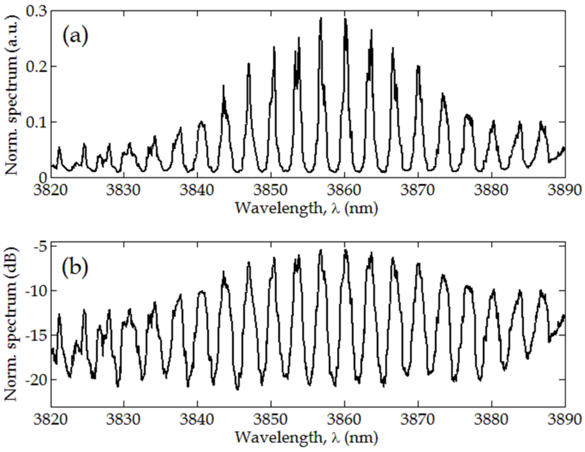

Fig. 4. Vernier #B spectra plotted in (a) a. u. and (b) dB scale.

Figure 3 shows the theoretical and experimental spectra of Vernier #A architecture. The theoretical Vernier transmittance is plotted in Fig. 3(a) in the wavelength range of 3.35-4 µm together with a plot of the experimental spectrum measured in the range of 3.790-3.889 µm. It is worth specifying that, although our tunable QCL can emit in the 3.7-3.9 µm range, fiber optic absorption and grating coupler transmission responses, limited the acquisition of the experimental data to a narrower spectrum. An enlarged view of the detected overall Vernier peak is plotted in arbitrary units (a.u.) and in a decibel (dB) scale in Figs. 3(b) and 3(c), respectively, where a very good agreement between theory and experiments can be seen. Moreover, figures of merit that characterize Vernier #A device are listed in Table 2, where the FSRs and power coupling coefficients, κ_c^2, of the cascade-coupled add-drop RRs have also been reported. In particular, insertion losses, IL_V, extinction ratios, ER_V, as well as Vernier loaded quality factors, Q_V, were evaluated at the central highest resonance of the overall Vernier peak. Finally, the successful operation in the second Vernier regime has been achieved as demonstrated by the shape of comb-like experimental spectra but also by the minimum $\Delta\lambda_{FWHM}$ equal to 2.31 nm and ΔFSR of 0.18 nm, which both satisfy Eq. (1).

Vernier #B architecture is characterized by RR lengths that are almost double the lengths of RR #A1 and RR #A2. As a consequence, the resulting FSR_V is ~ 81 nm, thus four times shorter than the FSR_V of Vernier #A device. A further demonstration of this can be appreciated by comparing $\Delta\lambda_V$ values as listed in Table 2. Indeed, the spectral distance between two adjacent resonances is now reduced to ~ 3.1 nm, i.e., almost half of the Vernier #A device (~ 7.5 nm). The experimental Vernier #B spectrum, plotted in a. u. units and dB scale in Figs. 4(a) and 4(b), respectively, exhibits a Vernier peak that is clearly distinguishable in the narrower wavelength range of 3.82-3.89 µm. In particular, the product of cascade-coupled RRs transmittances can be observed at the left side of both Figs. 4(a) and 4(b), where RR resonances are slightly misaligned. Conversely, the complete overlap of cascaded RR transmittances is achieved at longer wavelengths, where uniformly shaped resonant peaks can be observed. Finally, fabrication tolerances of ± 20 nm can induce resonant dips/peak shifts, $\Delta\lambda$, of

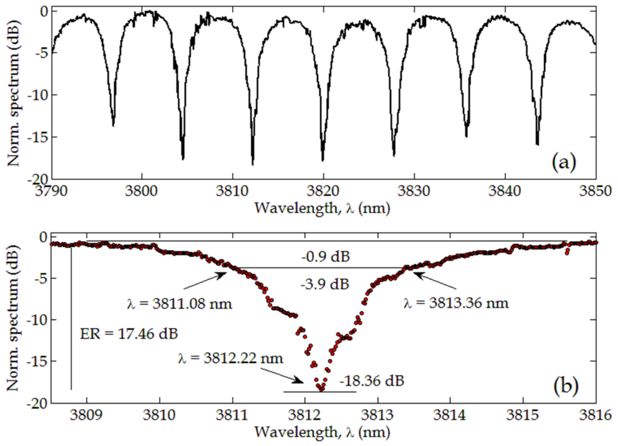

Fig. 5. (a) Ge-on-Si add-drop racetrack resonator spectrum. (b) A quality factor, *Q*, of ~ 1,700 can be seen.

maximum ± 2 nm, while maximum changes of power coupling coefficients, $\Delta\kappa_c^2$, can be ± 2.5×10^{-3}. The etch depth, *E*, is the most critical parameter.

As also reported in our previous work on the Vernier-effect in SOI devices operating in the MIR [13], RRs characterized by FSRs shorter than 5 nm and narrow resonant dips/peaks, which can be achieved when power coupling coefficients are much lower than 0.1, are most suitable for obtaining comb-like Vernier spectra characterized by high extinction ratios, ER_V. However, such a condition usually makes the characterization of single add-drop RR spectra quite challenging because of the presence of clipped resonances due to the mode-hopping behavior of the QCL commercial source used in our setup. As a consequence, in order to characterize a single Ge-on-Si RR, we have fabricated RR #A1 device, i.e., the RR that exhibits the longest FSR, characterized by a directional coupler gap, g_0, equal to 250 nm and the remaining dimensions identical to those reported in Table 1. In this way, power coupling coefficients of 0.098 have resulted, being almost twice that of the previous case, i.e., 0.042. Then, the add-drop RR based on the Ge-on-Si rib waveguide operating around 3.8 µm has been characterized and its spectrum is plotted in Fig. 5. An average insertion loss, IL ~ 1 dB, a maximum extinction ratio, ER = 17.46 dB, and a FSR of 7.7 nm can be seen in Fig. 5(a), while the maximum quality factor, *Q* = 1,672, is shown in Fig. 5(b). It is worth specifying that RRs presented in this Letter were not designed and optimized to operate in the critical coupling condition, thus to exhibit high quality factors, as this condition is not required for the design of Vernier devices operating in the second regime of the Vernier effect. In fact, greater *Q*-factors have previously been achieved in the MIR in other material platforms [20-23], with a record of 278,000 in silicon-on-sapphire RRs operating in the range of 4.3-4.6 µm [24].

In conclusion, it is worth noting that the Vernier gains achieved in Ge-on-Si cascade-coupled add-drop RRs operating at 3.8 µm, i.e., 43.44 and 25.46, are definitively better than the highest gains we measured in SOI Vernier devices at the same wavelength, i.e., 19.40 [13] and 19.94 [14]. In particular, by assuming a Vernier device with a gain $G_V \approx 44$ and RRs based on Ge waveguides optimized for sensing (e.g., suspended structures [25]), wavelength sensitivities up to ~40 µm/RIU and LODs of 10^{-4} RIU could be achieved at 3.8 µm. Sensing performance can be further enhanced by designing high-gain Vernier sensors based on highly sensitive waveguides.

The Ge-on-Si technology platform is more suitable than Ge-on-SOI for extending the operation of Vernier devices at wavelengths up to 14 µm, where SiO_2 exhibits a very strong absorption and requires the use of thick Si layers to achieve low loss. Actually, the reported design tools and fabrication processes can be used for extending the operation of Ge-on-Si Vernier devices to long MIR wavelengths, but a rigorous experimental investigation of bending losses is needed and the influence of Si optical absorption should be taken into account. Finally, it is worth specifying that small RR radii are not critical for achieving high Vernier gains and large RR lengths can be preferred to generate dense comb-like Vernier spectra, which are suitable for spectroscopy.

References

1. Y.-C. Chang, V. Paeder, L. Hvozdara, J.-M. Hartmann, and H. P. Herzig, Opt. Lett. **37**, 2883 (2012).
2. M. Nedeljkovic, J. Soler Penadés, C. J. Mitchell, A. Z. Khokhar, S. Stankovic, T. Dominguez Bucio, C. G. Littlejohns, F. Y. Gardes, and G. Z. Mashanovich, IEEE Photon. Technol. Lett. **27**, 1040 (2015).
3. A. Malik, M. Muneeb, Y. Shimura, J. Van Campenhout, R. Loo, and G. Roelkens, Appl. Phys. Lett. **103**, 161119 (2013).
4. A. Malik, M. Muneeb, S. Pathak, Y. Shimura, J. Van Campenhout, R. Loo, and G. Roelkens, IEEE Photon. Technol. Lett. **25**, 1805 (2013).
5. A. Malik, S. Dwivedi, L. Van Landschoot, M. Muneeb, Y. Shimura, G. Lepage, J. Van Campenhout, W. Vanherle, T Van Opstal, R. Loo, and G. Roelkens, Opt. Express **22**, 28479 (2014).
6. L. Shen, N. Healy, C. J. Mitchell, J. Soler Penadés, M. Nedeljkovic, G. Z. Mashanovich, and A. C. Peacock, Opt. Lett. **40**, 268 (2015).
7. L. Shen, N. Healy, C. J. Mitchell, J. Soler Penadés, M. Nedeljkovic, G. Z. Mashanovich, and A. C. Peacock, Opt. Lett. **40**, 2213 (2015).
8. M. Nedeljkovic, R. Soref, G. Z. Mashanovich, IEEE Photon. J. **7**, 2600214 (2015).
9. F. De Leonardis, B. Troia, R. A. Soref, and V. M. N. Passaro, Opt. Express **23**, 17237 (2015).
10. F. De Leonardis, B. Troia, R. A. Soref, and V. M. N. Passaro, J. Lightw. Technol. (in press).
11. G. Griffel, IEEE Photon. Technol. Lett. **12**, 1642 (2000).
12. B. Troia, A. Z. Khokhar, M. Nedeljkovic, S. A. Reynolds, Y. Hu, G. Z. Mashanovich, and V. M. N. Passaro, Sensors **15**, 13548 (2015).
13. B. Troia, A. Z. Khokhar, M. Nedeljkovic, J. Soler Penadés, V. M. N. Passaro, and G. Z. Mashanovich, Opt. Express **22**, 23990 (2014).
14. G. Z. Mashanovich, F. Y. Gardes, D. J. Thomson, Y. Hu, K. Li, M. Nedeljkovic, J. Soler Penadés, A. Z. Khokhar, C. J. Mitchell, S. Stankovic, R. Topley, S. A. Reynolds, Y. Wang, B. Troia, V. M. N. Passaro, C. G. Littlejohns, T. Dominguez Bucio, P. R. Wilson, and G. T. Reed, IEEE J. Sel. Topics Quantum Electron. **21**, 8200112 (2015).
15. Y.-C. Chang, P. Wägli, V. Paeder, A. Homsy, L. Hvozdara, P. Van Der Wal, J. Di Francesco, N. F. De Rooij, and H. P. Herzig, Lab Chip **12**, 3020 (2012).
16. V. M. N. Passaro, B. Troia, and F. De Leonardis, Sens. Actuators B Chem. **168**, 402 (2012).
17. B. Troia, F. De Leonardis, and V. M. N. Passaro, Opt. Lett. **39**, 1161 (2014).
18. H. H. Li, J. Phys. Chem. Ref. Data **9**, 561 (1980).
19. G. Z. Mashanovich, M. M. Milosevic, M. Nedeljkovic, N. Owens, B. Xiong, E. J. Teo, and Y. Hu, Opt. Express **19**, 7112 (2011).
20. Z. Cheng, X. Chen, C. Y. Wong, K. Xu, and H. K. Tsang, IEEE Photon. J. **4**, 1510 (2012).
21. H. Lin, L. Li, Y. Zou, S. Danto, J. D. Musgraves, K. Richardson, S. Kozacik, M. Murakowski, D. Prather, P. T. Lin, V. Singh, A. Agarwal, L. C. Kimerling, and J. Hu. Opt. Lett. **38**, 1470 (2013).
22. F. Jiang, N. Duan, H. Lin, L. Li, J. Hu, L. Bi, H. Lu, X. Weng, J. Xie, and L. Deng, Proc. SPIE **8988**, 89880S (2014).
23. P. Ma, D.-Y. Choi, Y. Yu, Z. Yang, K. Vu, T. Nguyen, A. Mitchell, B. Luther-Davies, and S. Madden, Opt. Express **23**, 19969 (2015).
24. R. Shankar, I. Bulu, and M. Lončar, Appl. Phys. Lett. **102**, 051108 (2013).
25. J. Soler Penadés, C. Alonso-Ramos, A. Z. Khokhar, M. Nedeljkovic, L. A. Boodhoo, A. Ortega-Moñux, I. Molina-Fernández, P. Cheben, and G. Z. Mashanovich, Opt. Lett. **39**, 5661 (2014).

References

1. Y.-C. Chang, V. Paeder, L. Hvozdara, J.-M. Hartmann, and H. P. Herzig, “Low-loss germanium strip waveguides on silicon for the mid-infrared,” Optics Letters, vol. 37, no. 14, pp. 2883-2885 (2012).
2. M. Nedeljkovic, J. Soler Penadés, C. J. Mitchell, A. Z. Khokhar, S. Stankovic, T. Dominguez Bucio, C. G. Littlejohns, F. Y. Gardes, and G. Z. Mashanovich, “Surface grating coupled low loss Ge-on-Si rib waveguides and multimode interferometers,” IEEE Photonics Technology Letters, vol. 27, no. 10, pp. 1040-1043 (2015).
3. A. Malik, M. Muneeb, Y. Shimura, J. Van Campenhout, R. Loo, and G. Roelkens, “Germanium-on-silicon planar concave grating wavelength (de)multiplexers in the mid-infrared,” Applied Physics Letters, vol. 103, 161119-1 - 161119-4 (2013).
4. A. Malik, M. Muneeb, S. Pathak, Y. Shimura, J. Van Campenhout, R. Loo, and G. Roelkens, “Germanium-on-silicon mid-infrared arrayed waveguide grating multiplexers,” IEEE Photonics Technology Letters, vol. 25, no. 18, pp. 1805-1808 (2013).
5. A. Malik, S. Dwivedi, L. Van Landschoot, M. Muneeb, Y. Shimura, G. Lepage, J. Van Campenhout, W. Vanherle, T Van Opstal, R. Loo, and G. Roelkens, “Ge-on-Si and Ge-on-SOI thermo-optic phase shifters for the mid-infrared,” Optics Express, vol. 22, no. 23, pp. 28479-28488 (2014).
6. L. Shen, N. Healy, C. J. Mitchell, J. Soler Penadés, M. Nedeljkovic, G. Z. Mashanovich, and A. C. Peacock, “Mid-infrared all-optical modulation in germanium-on-silicon waveguides,” Optics Letters, vol. 40, no. 2, 268-271 (2015).
7. L. Shen, N. Healy, C. J. Mitchell, J. Soler Penadés, M. Nedeljkovic, G. Z. Mashanovich, and A. C. Peacock, “Two-photon absorption and all-optical modulation in germanium-on-silicon waveguides for the mid-infrared,” Optics Letters vol. 40, no. 10, pp. 2213-2216 (2015).
8. M. Nedeljkovic, R. Soref, G. Z. Mashanovich, “Predictions of free-carrier electroabsorption and electrorefraction in germanium,” IEEE Photonics Journal, vol. 7, no. 7, 2600214 (2015).
9. F. De Leonardis, B. Troia, R. A. Soref, and V. M. N. Passaro, “Investigation of germanium Raman lasers for the mid-infrared,” Optics Express, vol. 23, no. 13, pp. 17237-17254 (2015).
10. F. De Leonardis, B. Troia, R. A. Soref, and V. M. N. Passaro, “Modelling of supercontinuum generation in the germanium-on-silicon waveguided platform,” Journal of Lightwave Technology (in press).
11. G. Griffel, “Vernier effect in asymmetrical ring resonator arrays,” IEEE Photonics Technology Letters, vol. 12, no. 12, pp. 1642-1644 (2000).
12. B. Troia, A. Z. Khokhar, M. Nedeljkovic, S. A. Reynolds, Y. Hu, G. Z. Mashanovich, and V. M. N. Passaro, “Design procedure and fabrication of reproducible silicon Vernier devices for high-performance refractive index sensing,” Sensors, vol. 15, no. 6, pp. 13548-13567 (2015).
13. B. Troia, A. Z. Khokhar, M. Nedeljkovic, J. Soler Penadés, V. M. N. Passaro, and G. Z. Mashanovich, “Cascade-coupled racetrack resonators based on the Vernier effect in the mid-infrared,” Optics Express, vol. 22, no. 20, pp. 23990-24003 (2014).
14. G. Z. Mashanovich, F. Y. Gardes, D. J. Thomson, Y. Hu, K. Li, M. Nedeljkovic, J. Soler Penadés, A. Z. Khokhar, C. J. Mitchell, S. Stankovic, R. Topley, S. A. Reynolds, Y. Wang, B. Troia, V. M. N. Passaro, C. G. Littlejohns, T. Dominguez Bucio, P. R. Wilson, and G. T. Reed, “Silicon photonic waveguides and devices for near- and mid-IR applications,” IEEE Journal of Selelected Topics in Quantum Electronics, vol. 21, no. 4, 8200112 (2015).
15. Y.-C. Chang, P. Wägli, V. Paeder, A. Homsy, L. Hvozdara, P. Van Der Wal, J. Di Francesco, N. F. De Rooij, and H. P. Herzig, “Cocaine detection by a mid-infrared waveguide integrated with a microfluidic chip,” Lab Chip, vol. 12, pp. 3020-3023 (2012).
16. V. M. N. Passaro, B. Troia, and F. De Leonardis, “A generalized approach for design of photonic gas sensors based on Vernier-effect in mid-IR,” Sensors and Actuators B: Chemical, vol. 168, pp. 402-420 (2012).
17. B. Troia, F. De Leonardis, and V. M. N. Passaro, “Generalized modelling for the design of guided-wave optical directional couplers,” Optics Letters, vol. 39, no. 5, 1161-1164 (2014).
18. H. H. Li, “Refractive index of silicon and germanium and its wavelength and temperature derivatives,” Journal of Physical and Chemical Reference Data, vol. 9, no. 3, pp. 561-658 (1980).
19. G. Z. Mashanovich, M. M. Milosevic, M. Nedeljkovic, N. Owens, B. Xiong, E. J. Teo, and Y. Hu, “Low loss silicon waveguides for the mid-infrared,” Optics Express, vol. 19, no. 8, pp. 7112-7119 (2011).
20. Z. Cheng, X. Chen, C. Y. Wong, K. Xu, and H. K. Tsang, “Mid-infrared suspended membrane waveguide and ring resonator on silicon-on-insulator,” IEEE Photonics Journal, vol. 4, no. 5, pp. 1510-1519 (2012).
21. H. Lin, L. Li, Y. Zou, S. Danto, J. D. Musgraves, K. Richardson, S. Kozacik, M. Murakowski, D. Prather, P. T. Lin, V. Singh, A. Agarwal, L. C. Kimerling, and J. Hu., “Demonstration of high-Q mid-infrared chalcogenide glass-on-silicon resonators,” Optics Letters, vol. 38, no. 9, pp. 1470-1472 (2013).
22. F. Jiang, N. Duan, H. Lin, L. Li, J. Hu, L. Bi, H. Lu, X. Weng, J. Xie, and L. Deng, “ZrO_2-TiO_2 thin films and resonators for mid-infrared integrated photonics,” Proceedings of SPIE 8988, 89880S (2014).
23. P. Ma, D.-Y. Choi, Y. Yu, Z. Yang, K. Vu, T. Nguyen, A. Mitchell, B. Luther-Davies, and S. Madden, “High Q factor chalcogenide ring resonators for cavity-enhanced MIR spectroscopic sensing,” Optics Express, vol. 23, no. 15, pp. 19969-19979 (2015).
24. R. Shankar, I. Bulu, and M. Lončar, “Integrated high-quality factor silicon-on-sapphire ring resonators for the mid-infrared,” Applied Physics Letters, vol. 102, 051108-1 - 051108-3 (2013).
25. J. Soler Penadés, C. Alonso-Ramos, A. Z. Khokhar, M. Nedeljkovic, L. A. Boodhoo, A. Ortega-Moñux, I. Molina-Fernández, P. Cheben, and G. Z. Mashanovich, “Suspended SOI waveguide with sub-wavelength grating cladding for mid-infrared,” Optics Letters, vol. 39, no. 19, pp. 5661-5664 (2014).